Universität Karlsruhe (TH)
Institut für Baustatik

A Robust Non-Linear Solid Shell Element Based on a Mixed Variational Formulation

S. Klinkel, F. Gruttmann, W. Wagner

Mitteilung 2(2004)

Universität Karlsruhe (TH)
Institut für Baustatik

A Robust Non-Linear Solid Shell Element Based on a Mixed Variational Formulation

S. Klinkel, F. Gruttmann, W. Wagner

Mitteilung 2(2004)

Prof. Dr.–Ing. W. Wagner
Institut für Baustatik
Universität Karlsruhe
Postfach 6980
76128 Karlsruhe

Telefon: (0721) 608–2280
Telefax: (0721) 608–6015
E–mail: bs@.uni-karlsruhe.de
Internet: http://www.bs.uni-karlsruhe.de

A Robust Non-Linear Solid Shell Element Based on a Mixed Variational Formulation

Sven Klinkel [a], Friedrich Gruttmann [b], Werner Wagner [a]

[a] *Institut f. Baustatik, Universität Karlsruhe (TH), Kaiserstr. 12, 76131 Karlsruhe, Germany*

[b] *Institut f. Werkstoffe u. Mechanik im Bauwesen, Technische Universität Darmstadt, Alexanderstr. 7, 64283 Darmstadt, Germany*

Abstract

The paper is concerned with a geometrically non-linear solid shell finite element formulation, which is based on the Hu-Washizu variational principle. For the approximation of the independent displacement, stress and strain fields, the strain field is additively decomposed into two parts. Due to the fact that one part of the strain field is interpolated in the same manner as proposed by the enhanced assumed strain (EAS) method, it is denoted as EAS field. The other strain field is approximated with the same interpolation functions as the stress field. In contrast to the EAS concept the approximation spaces of the stresses and the enhanced assumed strains are not orthogonal. Consequently the stress field is not eliminated from the finite element equations. For the displacements tri-linear shape functions are considered. Shear locking and curvature thickness locking are treated using assumed natural strain interpolations. A static condensation leads to a simple low order hexahedral solid shell element. Numerical tests show that the present model is very robust and allows larger load steps than an EAS solid shell element.

Key words: solid shell element, mixed finite element formulation, geometrically non-linear, finite strains
PACS:

1 Introduction

In engineering design shell structures are found in a wide range of applications, e.g. in civil engineering for bridges and roofs, in the automobile industry to model the body of cars and for smart materials and structures to analyze for example layered piezoelectric devices. Often a three dimensional material law is necessary to analyze such structures in detail. In particular in the region of

boundaries and loading points the transverse shear and thickness strains are not negligible anymore. Furthermore the interlaminar stresses in composites play an important role for the delamination analysis, see e.g. [37]. It is therefore worthwhile to develop shell elements using 3D material laws, in which this paper is a contribution to analyze thin shell structures with a surface oriented low order hexahedral solid shell element incorporating 3D material models.

In the past several shell elements have been developed, which include 3D constitutive relations between stresses and strains in the underlying variational formulation. For this class of shell elements one may distinguish between shell formulations which model a reference surface of shells, see e.g. [2, 5, 7, 9, 36] and solid shell formulations which model the top and bottom surface of shells, see e.g. [10, 14, 19, 23, 29, 42].

To improve the in-plane bending behavior usually the EAS method is applied to both types of shell formulations, see e.g. [2,5,9,14,19,42]. The EAS method was introduced by Simo and Rifai [35] and is based on a three field functional of the Hu-Washizu type. In [35] it is assumed that the stress and the enhanced assumed strain interpolations are orthogonal, which results in an elimination of the stress field from the finite element equations.

Stress approximations which are not eliminated on element level are used in hybrid stress element formulations. These mixed finite element formulations are based on the two field Hellinger-Reissner principle, see e.g. [24,30,38]. In [6] it is shown that the enhanced assumed strain concept and the hybrid stress method lead to identical finite elements. Another formulation which considers a stress field approximation was proposed in [12, 13, 26, 27]. In [12] a brick element is derived with a mixed enhanced strain method. On the basis of the Hu-Washizu principle displacements, stresses and strains are approximated on element level. To improve the performance for nearly incompressible regions an enhanced strain field is added. In accordance with [35] it is assumed that the stress and the enhanced assumed strain interpolations are orthogonal, which results in an elimination of some terms from the finite element equations. In [26, 27] a modified Hu-Washizu functional is introduced, which includes assumed strains and stresses and in addition a so called enhanced strain field. On the basis of this functional plane elasticity problems are analyzed.

In this paper we improve the element behavior by employing the Hu-Washizu functional, which includes a displacement field an assumed strain field and an assumed stress field. For approximation purposes the assumed strain field is additively decomposed into two parts. Due to the fact that one strain field is approximated in the same manner as the enhanced assumed strain field proposed in [35], we call it enhanced assumed strain field. In contrast to [12, 35], the independent stress and the enhanced assumed strain interpolations are not assumed to be orthogonal. Thus the independent stress field does not vanish

from the finite element equations. The independent stress and strain fields are interpolated with the same functions. This leads to an element formulation with a superior in-plane bending behavior for linear and non-linear applications. Here, we present a geometrically non-linear solid shell formulation, which is based on the Green-Lagrangean strain measure. To improve the non-linear behavior for thin shells and to obtain good results for distorted meshes in plate bending problems special assumed natural strain (ANS) interpolations are employed.

For shell structures with bending dominated loading we are focussing on three locking effects, transverse shear locking, curvature thickness locking and the Poisson thickness locking, which are discussed in the literature. The transverse shear locking is treated by applying the ANS interpolations to the transverse shear strains. Assumed natural strain interpolations were presented in [8, 11, 17]. The curvature thickness locking occurs in shell formulations incorporating a 3D material law due to artificial thickness strains. This effect was observed by Ramm et al. [28]. The curvature thickness locking is reduced by an ANS interpolation, which was proposed by Betsch and Stein [3]. To relieve the Poisson thickness locking a linear distribution of the transversal thickness strains is mandatory. Parisch [23] approximated the displacements with a quadratic interpolation through the thickness. Another method was proposed in [7], where a tri-linear distribution of the thickness strain is suggested by the EAS concept. Vu-Quoc and Tan [42] pointed out that the linear and the bi-linear terms are sufficient to pass the out-of-plane bending patch test.

In the present element development we consider also the enhanced assumed strain field to reduce the Poisson thickness locking. Over all the enhanced assumed strains are applied to the thickness strains and to the membrane strains, which leads to seven EAS parameters. The curvature thickness locking is treated by applying the ANS interpolation [3] to the Green-Lagrange thickness strain. To relieve the transverse shear locking we follow the approach of Dvorkin and Bathe [8]. The essential features of the present formulation are summarized as follows:

i) The variational principle is based on the Hu-Washizu functional. This leads on element level to the interpolation of the displacement, the assumed stress and strain fields. Here the strains are additively decomposed into two parts, where the approximation of these fields belonging to two different function spaces.
ii) To prevent the Poisson thickness locking three EAS parameters are chosen to enhance the transverse thickness strain.
iii) The transverse shear and thickness strains of the Green-Lagrange type are approximated with the ANS interpolations.
iv) The static condensation on element level yields a simple low order hexahe-

dral solid shell element formulation with eight nodes and three displacement degrees of freedom per node.

Within this features the most striking characteristics of the present solid shell element are:

i) A superior in-plane bending behavior within distorted meshes. Some linear and non-linear numerical examples show that the present element produces a more accurate displacement response than that of shell elements which are based on the enhanced assumed strain concept.
ii) The robustness of the formulation with respect to the size of the load step. Numerical examples demonstrate that even for huge load steps the present element needs much less equilibrium iterations to obtain convergence than shell formulations, which employ the standard enhanced assumed strain concept.

The outline of the paper is as follows: In Section 2 we introduce the geometrically non-linear kinematic assumption in a curvilinear description. The variational principle is introduced in Section 3. In Section 4 the mixed finite element approximation is presented. In Section 5 some numerical examples demonstrate the applicability for geometrically and physically non-linear examples at finite strains.

2 Kinematics

In this section the kinematics of the shell is briefly discussed using convective curvilinear co-ordinates. A convective description is necessary due to the ANS interpolations for the transverse shear and thickness strains. We introduce ξ^3 as thickness co-ordinate and ξ^1, ξ^2 as in-plane co-ordinates of the considered shell formulation. The position vectors of the reference configuration $\mathcal{B}_0$ and the current configuration $\mathcal{B}_t$ are denoted by $\boldsymbol{X}$ and $\boldsymbol{x} = \boldsymbol{X} + \boldsymbol{u}$, respectively.Here, $\boldsymbol{u}$ denotes the displacement vector of a point in the shell domain. The covariant tangent vectors are obtained by partial derivatives of the position vectors with respect to the convective co-ordinates ξ^i

$$\boldsymbol{G}_i = \frac{\partial \boldsymbol{X}}{\partial \xi^i} \ , \qquad \boldsymbol{g}_i = \frac{\partial \boldsymbol{x}}{\partial \xi^i} \ , \qquad i = 1,2,3 \quad , \tag{1}$$

whereas the contravariant basis vectors are defined in a standard manner by $\boldsymbol{G}_i \cdot \boldsymbol{G}^j = \delta_i^j$ and $\boldsymbol{g}_i \cdot \boldsymbol{g}^j = \delta_i^j$. The deformation gradient is a map of the tangent spaces $\boldsymbol{F}(\boldsymbol{X}) : \boldsymbol{T}\mathcal{B}_0 \rightarrow \boldsymbol{T}\mathcal{B}_t$ and is given in convective description as

$$\boldsymbol{F} = \frac{\partial \boldsymbol{x}}{\partial \boldsymbol{X}} = \boldsymbol{g}_i \otimes \boldsymbol{G}^i \quad , \tag{2}$$

where the summation convention on repeated indices is assumed. With the metric coefficients of the current configuration $g_{ij} = \boldsymbol{g}_i \cdot \boldsymbol{g}_j$ and of the reference configuration $G_{ij} = \boldsymbol{G}_i \cdot \boldsymbol{G}_j$ the Green-Lagrangean strain tensor reads

$$\boldsymbol{E} = E_{ij}\, \boldsymbol{G}^i \otimes \boldsymbol{G}^j \quad \text{with} \quad E_{ij} = \frac{1}{2}\left(g_{ij} - G_{ij}\right) \quad . \tag{3}$$

3 Variational formulation

Fundamental for the finite element formulation is the variational functional, for which stationarity is required. In this section the Hu-Washizu three-field functional is used. From the first variation of the functional the weak form and the local Euler-Lagrange partial differential equations are derived. Due to nonlinearity the weak form is solved iteratively. For this purpose the linearization of the weak form is provided. We start with the introduction of the functional

$$\Pi(\boldsymbol{u},\, \widehat{\boldsymbol{S}},\, \bar{\boldsymbol{E}}) = \int_{\mathcal{B}_0} \left(W_0(\bar{\boldsymbol{E}}) + \widehat{\boldsymbol{S}} : (\boldsymbol{E} - \bar{\boldsymbol{E}}) - \boldsymbol{u} \cdot \boldsymbol{b} \right) \mathrm{dV} - \int_{\partial_\sigma \mathcal{B}_0} \boldsymbol{u} \cdot \boldsymbol{t}\, \mathrm{dA} \quad , \tag{4}$$

where the assumed stress $\widehat{\boldsymbol{S}}$ and the assumed strain $\bar{\boldsymbol{E}}$ are work conjugate quantities in a material description. The stored energy function W_0 is a function of the assumed strain $\bar{\boldsymbol{E}}$. The load $\boldsymbol{b}$ is defined in the body $\mathcal{B}_0$ and $\boldsymbol{t}$ is the prescribed traction vector on the boundary $\partial_\sigma \mathcal{B}_0$ of the reference configuration. As usual we assume that $\partial \mathcal{B}_0 = \partial_\sigma \mathcal{B}_0 \cup \partial_u \mathcal{B}_0$, where $\partial_u \mathcal{B}_0$ denotes the boundary with prescribed values for $\boldsymbol{u}$. Let $\mathcal{V}$ be the space of admissible displacement variations defined as $\mathcal{V} := \{\delta \boldsymbol{u} \in [H^1(\mathcal{B}_0)]^3 \delta \boldsymbol{u}|_{\partial_u \mathcal{B}_0} = 0\}$. Further let $\mathcal{S}$ and $\mathcal{E}$ the spaces of admissible stress and strain variations given as $\mathcal{S} = \mathcal{E} = [L_2(\mathcal{B}_0)]$. The first variation with respect to the independent variables $(\boldsymbol{u},\, \widehat{\boldsymbol{S}},\, \bar{\boldsymbol{E}}) \in \mathcal{V} \times \mathcal{S} \times \mathcal{E}$ reads

$$\begin{aligned} \delta\Pi(\boldsymbol{u},\, \widehat{\boldsymbol{S}},\, \bar{\boldsymbol{E}}) = & \int_{\mathcal{B}_0} \left(\delta \boldsymbol{E} : \widehat{\boldsymbol{S}} - \delta \boldsymbol{u} \cdot \boldsymbol{b} \right) \mathrm{dV} - \int_{\partial_\sigma \mathcal{B}_0} \delta \boldsymbol{u} \cdot \boldsymbol{t}\, \mathrm{dA} \\ & + \int_{\mathcal{B}_0} \left(\delta \widehat{\boldsymbol{S}} : (\boldsymbol{E} - \bar{\boldsymbol{E}}) \right) \mathrm{dV} \\ & + \int_{\mathcal{B}_0} \left(\delta \bar{\boldsymbol{E}} : (\frac{\partial W_0}{\partial \bar{\boldsymbol{E}}} - \widehat{\boldsymbol{S}}) \right) \mathrm{dV} \;=\; 0 \quad . \end{aligned} \tag{5}$$

The variation of the Green-Lagrange strains is obtained as $\delta \boldsymbol{E} = \frac{1}{2}(\delta \boldsymbol{g}_i \cdot \boldsymbol{g}_j + \boldsymbol{g}_i \cdot \delta \boldsymbol{g}_j)\, \boldsymbol{G}^i \otimes \boldsymbol{G}^j$ with $\delta \boldsymbol{g}_i = \frac{\partial \delta \boldsymbol{u}}{\partial \xi^i}$. Integration by parts and the use of the divergence theorem in Eq. (5) yields the local Euler-Lagrange equations

$$\div(\boldsymbol{F}\widehat{\boldsymbol{S}}) + \boldsymbol{b} = \boldsymbol{0}\,, \quad \boldsymbol{E} - \bar{\boldsymbol{E}} = \boldsymbol{0}\,, \quad \frac{\partial W_0}{\partial \bar{\boldsymbol{E}}} - \widehat{\boldsymbol{S}} = \boldsymbol{0} \qquad \text{in } \mathcal{B}_0 \tag{6}$$

$$\boldsymbol{F}\widehat{\boldsymbol{S}}\,\bar{\boldsymbol{N}} = \boldsymbol{t} \qquad \text{on } \partial_\sigma \mathcal{B}_0 \quad . \tag{7}$$

Eq. $(6)_1$ represents the equilibrium condition, whereas the second equation is the geometrical field equation and the third equation describes the constitutive relation. Equation (7) ensures the boundary condition for a given traction on $\partial_\sigma \mathcal{B}_0$, where $\bar{\boldsymbol{N}}$ is the outward normal vector. It is remarked that within Eq. (5) the Euler-Lagrange equations are fulfilled in a weak sense. The remaining equation is the geometrical boundary condition $\boldsymbol{u} = \bar{\boldsymbol{u}}$ on $\partial_u \mathcal{B}$, which is a constraint.

It is noted that, if the space of the stress and strain fields are $L_2(\mathcal{B}_0)$ no inter-element continuity has to be enforced when constructing the finite element approximations.

The weak form is with respect to the Green-Lagrangean strain measure non-linear in the displacements and for more sophisticated materials the strain energy function W_0 is a non-linear function of the strains. To solve this equation iteratively within the finite element method the weak form is expanded in a Taylor series, which is truncated after the linear element $\delta\Pi^{k+1} = \delta\Pi^k + \mathrm{D}[\delta\Pi^{\mathrm{k}}] \cdot (\Delta\boldsymbol{u}, \Delta\widehat{\boldsymbol{S}}, \Delta\bar{\boldsymbol{E}}) \approx 0$. The superscript k denotes the iteration step. The linearization of the weak form results in

$$\begin{aligned} \mathrm{D}[\delta\Pi] \cdot (\Delta\boldsymbol{u}, \Delta\widehat{\boldsymbol{S}}, \Delta\bar{\boldsymbol{E}}) = & \int_{\mathcal{B}_0} \left(\Delta\delta\boldsymbol{E} : \widehat{\boldsymbol{S}} + \delta\boldsymbol{E} : \Delta\widehat{\boldsymbol{S}} \right) \mathrm{dV} \\ & + \int_{\mathcal{B}_0} \left(\delta\bar{\boldsymbol{E}} : \frac{\partial\partial W_0}{\partial\bar{\boldsymbol{E}}\partial\bar{\boldsymbol{E}}} : \Delta\bar{\boldsymbol{E}} - \delta\bar{\boldsymbol{E}} : \Delta\widehat{\boldsymbol{S}} \right) \mathrm{dV} \\ & + \int_{\mathcal{B}_0} \left(\delta\widehat{\boldsymbol{S}} : \Delta\boldsymbol{E} - \delta\widehat{\boldsymbol{S}} : \Delta\bar{\boldsymbol{E}} \right) \mathrm{dV} \quad . \end{aligned} \tag{8}$$

The linearized virtual Green-Lagrangean strain tensor reads $\Delta\delta\boldsymbol{E} = \frac{1}{2}(\delta\boldsymbol{g}_i \cdot \Delta\boldsymbol{g}_j + \Delta\boldsymbol{g}_i \cdot \delta\boldsymbol{g}_j)\, \boldsymbol{G}^i \otimes \boldsymbol{G}^j$.

4 Mixed finite element approximation

In this section an eight node solid shell element is derived. The finite element approximation is constructed in the sense that the whole domain is divided in element domains with $\mathcal{B} = \cup_{e=1}^{nelm} \mathcal{B}_e$, where $nelm$ is the total number of elements. By means of the isoparametric concept the approximations of the geometry and the displacements on element level (index e) are given by

$$\boldsymbol{X}_e^h = \boldsymbol{N}\, \boldsymbol{Y}_e \quad \text{and} \quad \boldsymbol{u}_e^h = \boldsymbol{N}\, \boldsymbol{v}_e \quad . \tag{9}$$

The vectors $\boldsymbol{Y} \in \mathbb{R}^{3\times 8}$, $\boldsymbol{v} \in \mathbb{R}^{3\times 8}$ contain the nodal co-ordinates and the nodal displacements, respectively. The superscript h is the characteristic size of the finite element discretization and indicates the finite element approximation.

The shape functions per node $I = 1, 2, 3, ..., 8$

$$N_I = \frac{1}{8}(1 + \xi_I^1 \xi^1)(1 + \xi_I^2 \xi^2)(1 + \xi_I^3 \xi^3) \quad \text{with} \quad -1 \leq \xi^i \leq +1 \tag{10}$$

are arranged in the matrix $\boldsymbol{N} = [\boldsymbol{N}_1, \boldsymbol{N}_2, \boldsymbol{N}_3, \boldsymbol{N}_4, \boldsymbol{N}_5, \boldsymbol{N}_6, \boldsymbol{N}_7, \boldsymbol{N}_8]$ with $\boldsymbol{N}_I = \text{diag}[N_I, N_I, N_I]$. The virtual displacement vector $\delta \boldsymbol{u}$ is interpolated in the same manner as the displacement vector

$$\delta \boldsymbol{u}_e^h = \boldsymbol{N}\, \delta \boldsymbol{v}_e \quad , \tag{11}$$

where $\delta \boldsymbol{v}_e$ is the virtual nodal displacement vector. Following common usage in the finite element literature we order the cartesian coefficients of $\boldsymbol{E}$ in a vector $\boldsymbol{E} = [E_{11}, E_{22}, E_{33}, 2E_{12}, 2E_{13}, 2E_{23}]^T$. For the approximation of the Green-Lagrangean strain components on element level some assumed natural strain (ANS) interpolations are employed. This is necessary to reduce transverse shear locking and to circumvent curvature thickness locking. The ANS interpolations require a convective description. The approximation of the covariant basis vectors are given as

$$\boldsymbol{G}_i^h = \boldsymbol{N}_{,i}\, \boldsymbol{Y}_e \quad , \quad \boldsymbol{g}_i^h = \boldsymbol{N}_{,i}\, (\boldsymbol{Y}_e + \boldsymbol{v}_e) \quad , \tag{12}$$

where $\boldsymbol{N}$ is differentiated with respect to ξ^i. Accordingly the metric coefficients read

$$G_{ij}^h = \boldsymbol{G}_i^h \cdot \boldsymbol{G}_j^h \quad , \quad g_{ij}^h = \boldsymbol{g}_i^h \cdot \boldsymbol{g}_j^h \quad . \tag{13}$$

The transformation of the Green-Lagrangean strain components (3) to cartesian co-ordinates is obtained by the matrix $\boldsymbol{T}_S^{-T}$. To define $\boldsymbol{T}_S$ we introduce

$$\boldsymbol{T} = \begin{bmatrix} (J_{11})^2 & (J_{12})^2 & (J_{13})^2 & aJ_{11}J_{12} & aJ_{11}J_{13} & aJ_{12}J_{13} \\ (J_{21})^2 & (J_{22})^2 & (J_{23})^2 & aJ_{21}J_{22} & aJ_{21}J_{23} & aJ_{22}J_{23} \\ (J_{31})^2 & (J_{32})^2 & (J_{33})^2 & aJ_{31}J_{32} & aJ_{31}J_{33} & aJ_{32}J_{33} \\ bJ_{11}J_{21} & bJ_{12}J_{22} & bJ_{13}J_{23} & J_{11}J_{22} + J_{12}J_{21} & J_{11}J_{23} + J_{13}J_{21} & J_{12}J_{23} + J_{13}J_{22} \\ bJ_{11}J_{31} & bJ_{12}J_{32} & bJ_{13}J_{33} & J_{11}J_{32} + J_{12}J_{31} & J_{11}J_{33} + J_{13}J_{31} & J_{12}J_{33} + J_{13}J_{32} \\ bJ_{21}J_{31} & bJ_{22}J_{32} & bJ_{23}J_{33} & J_{21}J_{32} + J_{22}J_{31} & J_{21}J_{33} + J_{23}J_{31} & J_{22}J_{33} + J_{23}J_{32} \end{bmatrix} , \tag{14}$$

where

$$\boldsymbol{T}_S = \boldsymbol{T} \quad \text{with} \quad a = 2 \quad \text{and} \quad b = 1\,. \tag{15}$$

The quantities J_{ik} are defined as $J_{ik} = \boldsymbol{e}_i \cdot \boldsymbol{G}_k$ where $\boldsymbol{e}_i$ describe the orthonormal basis vectors in cartesian co-ordinate space.

In accordance with [3] an ANS interpolation for the convective thickness strain is applied to overcome curvature thickness locking. The ANS interpolation considers four collocation points, which are defined in convective co-ordinates ξ^i

as $i = (-1,-1,0)$, $ii = (1,-1,0)$, $iii = (1,1,0)$ and $iv = (-1,1,0)$. Considering Eqs. (12), (13) the thickness strain is evaluated at these points and is interpolated bi-linear through the element. Values evaluated at the collocation points are denoted with superscript $L = i, ii, iii, iv$.

To reduce the transverse shear locking in the case of distorted element geometries the ANS interpolations proposed in [8] are applied. Therefore the four collocation points $A = (-1,0,0)$, $B = (0,-1,0)$, $C = (1,0,0)$, and $D = (0,1,0)$ are defined in convective co-ordinates ξ^i. Employing Eqs. (12), (13) the shear strains are evaluated at these points and denoted with the superscripts A, B, C and D, respectively.

Due to the ANS interpolations the brick element is not isotropic anymore. In particular, ξ^1, ξ^2 are now the in-plane co-ordinates and ξ^3 is the thickness co-ordinate of the present solid shell element. With respect to the ANS interpolations the approximation of the cartesian strain components read

$$\boldsymbol{E}_e^h = \boldsymbol{T}_S^{-T} \begin{bmatrix} \frac{1}{2}(g_{11}^h - G_{11}^h) \\ \frac{1}{2}(g_{22}^h - G_{22}^h) \\ \sum_{L=i}^{iv} \frac{1}{4}(1+\xi_L^1\xi^1)(1+\xi_L^2\xi^2)\, \frac{1}{2}(g_{33}^L - G_{33}^L) \\ (g_{12}^h - G_{12}^h) \\ (1-\xi^2)(g_{13}^B - G_{13}^B) + (1+\xi^2)(g_{13}^D - G_{13}^D) \\ (1-\xi^1)(g_{23}^A - G_{23}^A) + (1+\xi^1)(g_{23}^C - G_{23}^C) \end{bmatrix} \quad . \tag{16}$$

The approximation of the virtual Green-Lagrangean strains on element level is given by

$$\delta \boldsymbol{E}_e^h = \boldsymbol{B}\, \delta \boldsymbol{v} \quad \text{with} \quad \boldsymbol{B} = [\boldsymbol{B}_1,\, \boldsymbol{B}_2,\, \boldsymbol{B}_3,\, \boldsymbol{B}_4,\, \boldsymbol{B}_5,\, \boldsymbol{B}_6,\, \boldsymbol{B}_7,\, \boldsymbol{B}_8] \quad . \tag{17}$$

The matrix $\boldsymbol{B}_I$ at the node I is also specified by the ANS interpolations as

$$\boldsymbol{B}_I = \boldsymbol{T}_S^{-T} \begin{bmatrix} N_{I,1}\,\boldsymbol{g}_1^{hT} \\ N_{I,2}\,\boldsymbol{g}_2^{hT} \\ \sum_{L=i}^{iv}\ \frac{1}{4}(1+\xi_L^1\xi^1)(1+\xi_L^2\xi^2)\,N_{I,3}\,(\boldsymbol{g}_3^L)^T \\ N_{I,1}\,\boldsymbol{g}_2^{hT} + N_{I,2}\,\boldsymbol{g}_1^{hT} \\ (1-\xi^2)(N_{I,1}^B\,(\boldsymbol{g}_3^B)^T + N_{I,3}^B\,(\boldsymbol{g}_1^B)^T) + (1+\xi^2)(N_{I,1}^D\,(\boldsymbol{g}_3^D)^T + N_{I,3}^D\,(\boldsymbol{g}_1^D)^T) \\ (1-\xi^1)(N_{I,2}^A\,(\boldsymbol{g}_3^A)^T + N_{I,3}^A\,(\boldsymbol{g}_2^A)^T) + (1+\xi^1)(N_{I,2}^C\,(\boldsymbol{g}_3^C)^T + N_{I,3}^C\,(\boldsymbol{g}_2^C)^T) \end{bmatrix}. \tag{18}$$

For the incremental Green-Lagrangean strains the same interpolation as in (17) is applied, thus $\Delta\boldsymbol{E}_e^h = \boldsymbol{B}\,\Delta\boldsymbol{v}$. In the linearized weak form (8) the quantity $\Delta\delta\boldsymbol{E} : \widehat{\boldsymbol{S}}$ appears, which is approximated as

$$(\Delta\delta\boldsymbol{E} : \widehat{\boldsymbol{S}})^h = \delta\boldsymbol{v}_e^T\,\boldsymbol{G}\,\Delta\boldsymbol{v}_e \quad \text{with} \quad \boldsymbol{G} = \begin{bmatrix} \boldsymbol{G}_{11} & \boldsymbol{G}_{12} & \cdots & \boldsymbol{G}_{18} \\ \boldsymbol{G}_{21} & \boldsymbol{G}_{22} & \cdots & \boldsymbol{G}_{28} \\ \vdots & \vdots & \ddots & \vdots \\ \boldsymbol{G}_{81} & \boldsymbol{G}_{82} & \cdots & \boldsymbol{G}_{88} \end{bmatrix}, \tag{19}$$

where $\boldsymbol{G}_{IJ}$ is defined for a node combination I and J as $\boldsymbol{G}_{IJ} = \mathrm{diag}[G_{IJ},\, G_{IJ},\, G_{IJ}]$. Considering the ANS interpolations of [8] and [3] and the transformation (15) the scalar G_{IJ} is obtained as

$$G_{IJ} = (\widehat{\boldsymbol{S}}_e^h)^T\,\boldsymbol{T}_S^{-T} \begin{bmatrix} N_{I,1}N_{J,1} \\ N_{I,2}N_{J,2} \\ \sum_{L=i}^{iv}\ \frac{1}{4}(1+\xi_L^1\xi^1)(1+\xi_L^2\xi^2)\,N_{I,3}N_{J,3} \\ N_{I,1}N_{J,2} + N_{I,2}N_{J,1} \\ \frac{1}{2}[(1-\xi^2)\,(N_{I,1}^B N_{J,3}^B + N_{I,3}^B N_{J,1}^B) + (1+\xi^2)\,(N_{I,1}^D N_{J,3}^D + N_{I,3}^D N_{J,1}^D)] \\ \frac{1}{2}[(1-\xi^1)\,(N_{I,2}^B N_{J,3}^A + N_{I,3}^B N_{J,2}^A) + (1+\xi^1)\,(N_{I,2}^C N_{J,3}^C + N_{I,3}^C N_{J,2}^C)] \end{bmatrix}, \tag{20}$$

where $\widehat{\boldsymbol{S}}_e^h$ is the approximation of the stress field $\widehat{\boldsymbol{S}}$, which is organized in vector notation as $\widehat{\boldsymbol{S}} = [\widehat{S}_{11},\, \widehat{S}_{22},\, \widehat{S}_{33},\, \widehat{S}_{12},\, \widehat{S}_{13},\, \widehat{S}_{23}]^T$.

4.1 Interpolation of the assumed strain field

The strain tensor $\bar{\boldsymbol{E}}$ is additively decomposed in $\widehat{E}^{ij}\,\boldsymbol{G}_i \otimes \boldsymbol{G}_j$ and $\widetilde{E}_{ij}\,\boldsymbol{G}^i \otimes \boldsymbol{G}^j$, which reads

$$\bar{\boldsymbol{E}} = \widehat{\boldsymbol{E}} + \widetilde{\boldsymbol{E}} \quad . \tag{21}$$

For the approximation of the two fields different function spaces $\widehat{\mathcal{E}}^h = [L_2(\mathcal{B}_0)]$ and $\widetilde{\mathcal{E}}^h = [L_2(\mathcal{B}_0)]$ are considered.

Considering vector notation the contravariant components of the strain field $\widehat{\boldsymbol{E}}$ are interpolated and transformed to cartesian space. Along with the vector notation the cartesian components are obtained with the transformation matrix $\boldsymbol{T}_E$. According to Eq. (14) $\boldsymbol{T}_E$ is defined as $\boldsymbol{T}_E = \boldsymbol{T}$ with $a = 1$ and $b = 2$. Due to the fact that no inter-element continuity is required the approximations of the strain field is defined on element level as

$$\widehat{\boldsymbol{E}}_e^h = \widehat{\boldsymbol{N}}_E\,\widehat{\boldsymbol{\alpha}}_e \;, \quad \widehat{\boldsymbol{\alpha}}_e \in \mathbb{R}^{18} \quad \text{with} \quad \widehat{\boldsymbol{N}}_E = [\boldsymbol{T}_E^0 \;\; \boldsymbol{T}_E^0\widehat{\boldsymbol{N}} \;\; \boldsymbol{T}_E\widehat{\widehat{\boldsymbol{N}}}] \quad . \tag{22}$$

The interpolation matrices $\widehat{\boldsymbol{N}}$ and $\widehat{\widehat{\boldsymbol{N}}}$ are given as

$$\widehat{\boldsymbol{N}} = \begin{bmatrix} \xi^3 & \xi^2\xi^3 & 0 & 0 & 0 \\ 0 & 0 & \xi^3 & \xi^1\xi^3 & 0 \\ 0 & 0 & 0 & 0 & 0 \\ 0 & 0 & 0 & 0 & \xi^3 \\ 0 & 0 & 0 & 0 & 0 \\ 0 & 0 & 0 & 0 & 0 \end{bmatrix} \;, \; \widehat{\widehat{\boldsymbol{N}}} = \begin{bmatrix} \xi^2 & 0 & 0 & 0 & 0 & 0 & 0 \\ 0 & \xi^1 & 0 & 0 & 0 & 0 & 0 \\ 0 & 0 & \xi^1 & \xi^2 & \xi^1\xi^2 & 0 & 0 \\ 0 & 0 & 0 & 0 & 0 & 0 & 0 \\ 0 & 0 & 0 & 0 & 0 & \xi^2 & 0 \\ 0 & 0 & 0 & 0 & 0 & 0 & \xi^1 \end{bmatrix} \quad . \tag{23}$$

It is noted that constant values and values which are interpolated through the thickness $\widehat{\boldsymbol{N}}(\xi^1, \xi^2, \xi^3)$ are transformed to cartesian space with the constant transformation matrix $\boldsymbol{T}_E^0$, whereas values which are interpolated in plane $\widehat{\widehat{\boldsymbol{N}}}(\xi^1, \xi^2)$ are transformed with $\boldsymbol{T}_E$.

Fore the strain field $\widetilde{\boldsymbol{E}}$ the covariant components are interpolated and transformed to cartesian space in the same manner as proposed by Simo and Rifai [35]. Therefore we refer to $\widetilde{\boldsymbol{E}}$ as enhanced assumed strain field. The discontinuous finite element approximation is defined on element level as

$$\widetilde{\boldsymbol{E}}_e^h = \widetilde{\boldsymbol{M}}\,\widetilde{\boldsymbol{\alpha}}_e \;, \quad \widetilde{\boldsymbol{\alpha}}_e \in \mathbb{R}^7 \quad \text{with} \quad \widetilde{\boldsymbol{M}} = \frac{\det \boldsymbol{J}^0}{\det \boldsymbol{J}}\,(\boldsymbol{T}_S^0)^{-T}\,\boldsymbol{M} \quad . \tag{24}$$

The Jacobian matrix is given as $\boldsymbol{J} = [\boldsymbol{G}_1^h, \boldsymbol{G}_2^h, \boldsymbol{G}_3^h]^T$. The superscript 0 indicates that the quantity is evaluated at the center of the element. The interpo-

lation matrix $\boldsymbol{M}$ reads

$$\boldsymbol{M} = \begin{bmatrix} \xi^1 & \xi^1\xi^2 & 0 & 0 & 0 & 0 & 0 \\ 0 & 0 & \xi^2 & \xi^1\xi^2 & 0 & 0 & 0 \\ 0 & 0 & 0 & 0 & \xi^3 & \xi^1\xi^3 & \xi^2\xi^3 \\ 0 & 0 & 0 & 0 & 0 & 0 & 0 \\ 0 & 0 & 0 & 0 & 0 & 0 & 0 \\ 0 & 0 & 0 & 0 & 0 & 0 & 0 \end{bmatrix} \quad . \tag{25}$$

The interpolation of the total strain is summarized as

$$\bar{\boldsymbol{E}}_e^h = \boldsymbol{N}_E\,\boldsymbol{\alpha}_e \quad \text{with} \quad \boldsymbol{N}_E = \left[\,\widehat{\boldsymbol{N}}_E\ \widetilde{\boldsymbol{M}}\,\right] \ , \quad \boldsymbol{\alpha}_e = \begin{bmatrix} \widehat{\boldsymbol{\alpha}}_e \\ \widetilde{\boldsymbol{\alpha}}_e \end{bmatrix} \ , \quad \boldsymbol{\alpha}_e \in \mathbb{R}^{25} \quad . \tag{26}$$

The interpolation (26) is also applied for the virtual strains $\delta\bar{\boldsymbol{E}}_e^h = \boldsymbol{N}_E\,\delta\boldsymbol{\alpha}_e$ and the incremental strains $\Delta\bar{\boldsymbol{E}}_e^h = \boldsymbol{N}_E\,\Delta\boldsymbol{\alpha}_e$.

4.2 Interpolation of the assumed stress field

Let $\mathcal{S}^h$ be the approximation of the stress space $\mathcal{S}$. Along with the vector notation the discontinuous approximation of the stress field reads

$$\widehat{\boldsymbol{S}}_e^h = \boldsymbol{N}_S\,\boldsymbol{\beta}_e \ , \quad \boldsymbol{\beta}_e \in \mathbb{R}^{18} \quad \text{with} \quad \boldsymbol{N}_S = [\boldsymbol{T}_S^0 \ \ \boldsymbol{T}_S^0\widehat{\boldsymbol{N}} \ \ \boldsymbol{T}_S\widehat{\widehat{\boldsymbol{N}}}] \quad . \tag{27}$$

The interpolation matrices $\widehat{\boldsymbol{N}}$ and $\widehat{\widehat{\boldsymbol{N}}}$ are given with Eq. (23). For the approximation of the virtual stress $\delta\widehat{\boldsymbol{S}}_e^h$ and the incremental stress $\Delta\widehat{\boldsymbol{S}}_e^h$ the same interpolation (27) is applied.

Remark 1: The interpolation of the independent stress field is similar to the interpolation which is used for hybrid stress brick elements based on the Hellinger-Reissner principle, see [16,25,30]. These works differ in the transformation strategy of the 18 interpolation functions. However, here the constant stresses and the stresses which are interpolated in ξ^3 are transformed with the constant transformation matrix $\boldsymbol{T}_S^0$, whereas the stresses which are interpolated in ξ^1 and ξ^2 are transformed with $\boldsymbol{T}_S$. This is necessary to pass the relevant patch tests, see also section 5.1.

Remark 2: The finite element approximations of the stress space $\mathcal{S}^h$ and the enhanced assumed strain space $\hat{\mathcal{E}}^h$ are not supposed to be orthogonal. With Eqs. (24) and (27) one obtains on element level

$$\begin{aligned}
&\int_{\mathcal{B}_e} \widehat{\boldsymbol{S}}_e^h \cdot \widetilde{\boldsymbol{E}}_e^h \, \mathrm{dV_e} = \boldsymbol{\beta}_\mathrm{e}^\mathrm{T} \int_{\mathcal{B}_\mathrm{e}} \widehat{\boldsymbol{N}}_\mathrm{S}^\mathrm{T} \widetilde{\boldsymbol{M}} \, \mathrm{dV_e} \, \widetilde{\boldsymbol{\alpha}}_\mathrm{e} \\
&= \boldsymbol{\beta}_e^T \int_{\mathcal{B}_e} \left(\boldsymbol{M} + (\widehat{\boldsymbol{N}})^T \widetilde{\boldsymbol{M}} + (\widehat{\widehat{\boldsymbol{N}}})^T (\boldsymbol{T}_S)^T \, (\boldsymbol{T}_S^0)^{-T} \, \boldsymbol{M} \right) \frac{\det \boldsymbol{J}^0}{\det \boldsymbol{J}} \, \mathrm{dV_e} \, \widetilde{\boldsymbol{\alpha}}_\mathrm{e} \\
&= \boldsymbol{\beta}_e^T \int_{\mathcal{B}_e} \left((\widehat{\widehat{\boldsymbol{N}}})^T (\boldsymbol{T}_S)^T \, (\boldsymbol{T}_S^0)^{-T} \, \boldsymbol{M} \right) \mathrm{d}\xi^1 \mathrm{d}\xi^2 \mathrm{d}\xi^3 \, \widetilde{\boldsymbol{\alpha}}_\mathrm{e} \, \det \boldsymbol{J}^0 \, .
\end{aligned} \tag{28}$$

The integral only vanishes if $\boldsymbol{T}_S$ and $\boldsymbol{T}_S^0$ are identical, which is the case if the element geometry has the shape of a parallelepiped.

4.3 Approximation of the weak form and its linearization

Considering the above introduced interpolations in Eqs. (5) and (8) the element matrices

$$\begin{aligned}
\boldsymbol{K}_e &= \int_{\mathcal{B}_e} \boldsymbol{G} \, \mathrm{dV_e} & \boldsymbol{L}_e &= \int_{\mathcal{B}_e} \boldsymbol{N}_S^T \boldsymbol{B} \, \mathrm{dV_e} \\
\boldsymbol{A}_e &= \int_{\mathcal{B}_e} \boldsymbol{N}_E^T \frac{\partial \partial W_0}{\partial \bar{\boldsymbol{E}}_e^h \partial \bar{\boldsymbol{E}}_e^h} \boldsymbol{N}_E \, \mathrm{dV_e} & \boldsymbol{Q}_e &= \int_{\mathcal{B}_e} \boldsymbol{N}_S^T \boldsymbol{N}_E \, \mathrm{dV_e}
\end{aligned} \tag{29}$$

and the element vectors

$$\begin{aligned}
\boldsymbol{f}_e^{int} &= \int_{\mathcal{B}_e} \boldsymbol{B}^T \widehat{\boldsymbol{S}}_e^h \, \mathrm{dV_e} & \boldsymbol{f}_e^{ext} &= \int_{\mathcal{B}_e} \boldsymbol{N}^T \boldsymbol{b} \, \mathrm{dV_e} + \int_{\partial \mathcal{B}_\mathrm{e}} \boldsymbol{N}^\mathrm{T} \boldsymbol{t} \, \mathrm{dA_e} \\
\boldsymbol{a}_e &= \int_{\mathcal{B}_e} \boldsymbol{N}_E^T (\frac{\partial W_0}{\partial \bar{\boldsymbol{E}}_e^h} - \widehat{\boldsymbol{S}}_e^h) \, \mathrm{dV_e} & \boldsymbol{b}_e &= \int_{\mathcal{B}_e} \boldsymbol{N}_S^T (\boldsymbol{E}_e^h - \bar{\boldsymbol{E}}_e^h) \, \mathrm{dV_e}
\end{aligned} \tag{30}$$

are defined. Here the integrals are calculated by employing an Gauß integration scheme with $2 \times 2 \times 2$ integration points. With respect that Eq. (5) is solved iteratively with Newton's method the following approximation on element level is obtained

$$\begin{aligned}
&\left[\delta\Pi + \mathrm{D}[\delta\Pi] \cdot (\Delta \boldsymbol{u}, \, \Delta \widehat{\boldsymbol{S}}, \, \Delta \bar{\boldsymbol{E}}) \right]_e^h \Rightarrow \\
&\begin{bmatrix} \delta \boldsymbol{v}_e \\ \delta \boldsymbol{\alpha}_e \\ \delta \boldsymbol{\beta}_e \end{bmatrix}^T \left(\begin{bmatrix} \boldsymbol{f}_e^{int} - \boldsymbol{f}_e^{ext} \\ \boldsymbol{a}_e \\ \boldsymbol{b}_e \end{bmatrix} + \begin{bmatrix} \boldsymbol{K}_e & \boldsymbol{0} & \boldsymbol{L}_e^T \\ \boldsymbol{0} & \boldsymbol{A}_e & -\boldsymbol{Q}_e^T \\ \boldsymbol{L}_e & -\boldsymbol{Q}_e & \boldsymbol{0} \end{bmatrix} \begin{bmatrix} \Delta \boldsymbol{v}_e \\ \Delta \boldsymbol{\alpha}_e \\ \Delta \boldsymbol{\beta}_e \end{bmatrix} \right) .
\end{aligned} \tag{31}$$

Taking into account that the finite element interpolations for the strain field $\bar{\boldsymbol{E}}$ and the stress field $\widehat{\boldsymbol{S}}$ are discontinuous across the element boundaries a

static condensation on element level yields the element stiffness matrix and the right hand side as

$$\boldsymbol{K}_{Te} = \boldsymbol{K}_e + \boldsymbol{L}_e^T \, (\boldsymbol{Q}_e \, \boldsymbol{A}_e^{-1} \, \boldsymbol{Q}_e^T)^{-1} \, \boldsymbol{L}_e \tag{32}$$

$$\boldsymbol{f}_e = \boldsymbol{f}_e^{ext} - \boldsymbol{f}_e^{int} - \boldsymbol{L}_e^T \, (\boldsymbol{Q}_e \, \boldsymbol{A}_e^{-1} \, \boldsymbol{Q}_e^T)^{-1} (\boldsymbol{Q}_e \, \boldsymbol{A}_e^{-1} \, \boldsymbol{a}_e + \boldsymbol{b}_e) \quad . \tag{33}$$

After assembly over all elements $\boldsymbol{K}_T = \mathsf{A}_{e=1}^{nelm} \, \boldsymbol{K}_{Te}$, $\Delta \boldsymbol{V} = \mathsf{A}_{e=1}^{nelm} \, \Delta \boldsymbol{v}_e$ and $\boldsymbol{P} = \mathsf{A}_{e=1}^{nelm} \, \boldsymbol{f}_e$ one obtains a pure displacement problem

$$\boldsymbol{K}_T \, \Delta \boldsymbol{V} = \boldsymbol{P} \tag{34}$$

with the unknown incremental nodal displacements. The stresses and strains are updated with the increments

$$\Delta \boldsymbol{\beta}_e = (\boldsymbol{Q}_e \, \boldsymbol{A}_e^{-1} \, \boldsymbol{Q}_e^T)^{-1} (\boldsymbol{L}_e \Delta \boldsymbol{v}_e + \boldsymbol{Q}_e \, \boldsymbol{A}_e^{-1} \, \boldsymbol{a}_e + \boldsymbol{b}_e) \tag{35}$$

$$\Delta \boldsymbol{\alpha}_e = \boldsymbol{A}_e^{-1} \, (\boldsymbol{Q}_e^T \, \Delta \boldsymbol{\beta}_e - \boldsymbol{a}_e) \quad . \tag{36}$$

5 Numerical Examples

In this section we discuss the behavior of the present solid shell element formulation, which we call HSEE solid shell. The present formulations are compared with shell elements and with solid shell elements incorporating 3D material laws. Most of the formulations are based on the enhanced assumed strain concept to improve the membrane strains and the thickness strain. The shear locking and the curvature thickness locking are treated by ANS interpolations. A solid shell element which belongs to this class of formulations was proposed in [14,44]. Instead of the originally introduced five EAS parameters it is used in this paper with two additional parameters associated with the bilinear terms $\xi^1\xi^3$ and $\xi^2\xi^3$ for the thickness strains. In [42] it is shown that the element in this version is able to pass the out-of-plane bending patch test. Here we will refer to this element as Q1A3E7.

The following examples are calculated with an extended version of the program FEAP [39] and illustrate the superior behavior of the presented solid shell element.

5.1 Patch tests

The following numerical tests confirm that the presented element formulation is able to reproduce constant stress states for disturbed element geometries. Here we distinguish between the membrane patch test and the out of plane

bending patch test. In both tests we consider the element mesh illustrated in Fig. 1, which was introduced in [18]. Here E, ν, t are the Young's modulus, Poisson's ratio and the thickness of the plate.

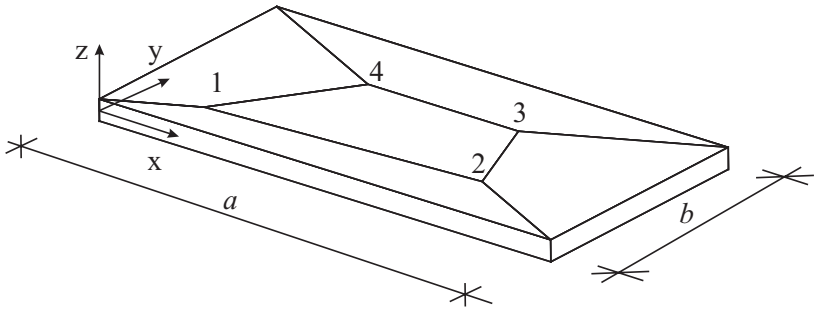

Geometry data:

$a = 0.24$

$b = 0.12$

$t = 0.001$

Material data:

$E = 10^6$

$\nu = 0.25$

Nodal co-ordinates: (x,y,z)

1 : (0.04, 0.02, 0.0005)

2 : (0.18, 0.03, 0.0005)

3 : (0.16, 0.08, 0.0005)

4 : (0.08, 0.08, 0.0005)

Fig. 1. Element mesh for the patch tests; 1, 2, 3, 4 are the numbers of the interior nodes on the top of the surface

5.1.1 Membrane patch tests

Following Vu-Quoc and Tan [42] the displacements

$$u_1 = (x + y/2) \cdot 10^{-3} \quad , \quad u_2 = (y + x/2) \cdot 10^{-3} \quad , \quad u_3 = 0.0 \tag{37}$$

are applied to the exterior nodes of the shell to obtain constant normal stress in x and y direction along with a constant shear stress in plane. A numerical solution of the problem with the present element formulation leads to constant values for the independent stress field

$$\widehat{S}_{11} = 1333 \quad , \quad \widehat{S}_{22} = 1333 \quad , \quad \widehat{S}_{12} = 400 \quad . \tag{38}$$

All other stress components are equal to zero. The results are in accordance with the analytical solution, which confirms that the membrane patch test is passed.

5.1.2 Out-of-plane bending patch test

The purpose of this test is to receive constant bending stresses. According to [42] the displacements

$$\begin{aligned} u_1 &= \mp\frac{h}{2}(x + y/2) \cdot 10^{-3} \\ u_2 &= \mp\frac{h}{2}(y + x/2) \cdot 10^{-3} \\ u_3 &= 10^{-3} \cdot (x^2 + xy + y^2)/2 \end{aligned} \tag{39}$$

at the top and bottom surface of the solid shell formulation have to be applied to the exterior nodes. The theoretical solution of the stresses at the top and bottom surface of the plate

$$\widehat{S}_{11} = \mp 0.6667 \quad , \quad \widehat{S}_{22} = \mp 0.6667 \quad , \quad \widehat{S}_{12} = \mp 0.200 \tag{40}$$

agrees exactly with the numerical solution obtained by the presented element formulation. For the HSEE solid shell element an evaluation of stresses at arbitrary points is possible due to the independent stress interpolations. This allows the calculation of stresses at e.g. the nodes of an element, whereas in standard displacement element formulations accurate values for the stresses are obtained only at the superconvergent points.

Node number	u_1	u_2	u_3
1	$-2.50 \cdot 10^{-8}$	$-2.00 \cdot 10^{-8}$	$1.400 \cdot 10^{-6}$
2	$-9.75 \cdot 10^{-8}$	$-6.00 \cdot 10^{-8}$	$1.935 \cdot 10^{-5}$
3	$-1.00 \cdot 10^{-7}$	$-8.00 \cdot 10^{-8}$	$2.240 \cdot 10^{-5}$
4	$-6.00 \cdot 10^{-8}$	$-6.00 \cdot 10^{-8}$	$9.600 \cdot 10^{-6}$

Table 1
Displacements at internal nodes, analytical solution

The displacements of the interior nodes are given by equation (39) and are summarized in Tab. 1. The values agree exactly with the displacements calculated with the presented HSEE solid shell element.

5.2 Bending tests

5.2.1 In-plane bending tests

This example is also a geometrical linear example in which in-plane shear locking with respect to mesh distortion is investigated. A cantilever beam is modelled with two finite elements and is subjected to a couple force F at its free end, see Fig. 2. Here the boundary conditions at the clamped end are

indicated with lines. The St.-Venant material is described with the Young's modulus E and the Poisson's ratio ν. The analytical solution yields a tip deflection of v = 1.

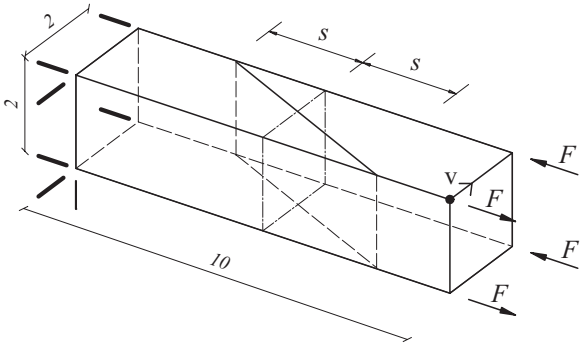

Loading:

$F = 10$

Material data:

$E = 1.5 \cdot 10^3$

$\nu = 0$

Fig. 2. Clamped beam loaded with a couple

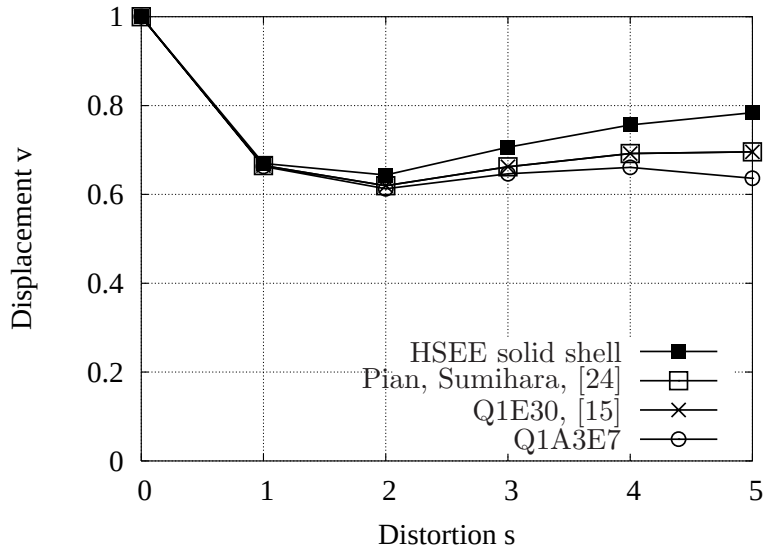

Fig. 3. Deflection v at the tip of the cantilever versus mesh distortion s

In Fig. 3 the displacement response v for different mesh distortion parameters s is shown. The solution of Pian and Sumihara [24] is often used as a reference with respect to sensitivity for in-plane mesh distortion, see e.g. [35]. The plane stress element in [24] is based on the Hellinger-Reissner variational principle. The response of the Q1A3E7 element with 7 EAS parameters leads to slightly smaller deflections than obtained with [24]. One obtains similar results as [24], if more EAS parameters are used. This is the case with the brick element Q1E30, which utilize 30 EAS parameters, see [15]. The results calculated with the HSEE solid shell element are the best among the considered elements.

5.2.2 Plate bending test

An often used linear example to investigate the mesh sensitivity in plate bending problems is the clamped square plate subjected to a single load, see Fig. 4. The St.-Venant Kirchhoff material is defined by material parameters E and ν and the thickness of the plate is $t = 1$. Considering symmetry only a quarter of the system is discretized with one layer of 2×2 elements. An analytical solution based on the Kirchhoff theory is provided in [40] as

$$w = 0.00560\, FL^2\, \frac{12(1-\nu^2)}{Eh^3} = 1 \quad . \tag{41}$$

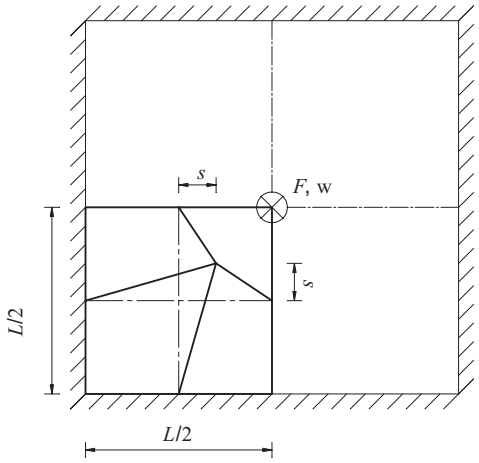

Geometry:

$L = 100$

Loading:

$F = 16.3527$

Material data:

$E = 1 \cdot 10^4$

$\nu = 0.3$

Fig. 4. Clamped plate with single load and finite element model

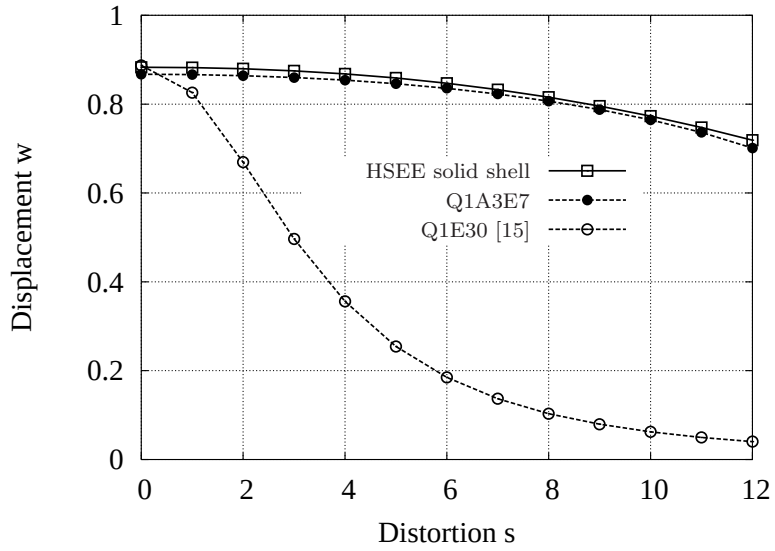

Fig. 5. Deflection w at the middle of the plate versus mesh distortion s

In Fig. 5 the center deflection for different distortion parameters is depicted. It is noted that both solid shell elements HSEE and Q1A3E7 show a similar distortion sensitivity. These elements are much more robust against mesh

distortion than the EAS brick element Q1E30. The reason for the good behavior of the solid shell elements is the ANS interpolation for the transverse shear strains, which reduces the transverse shear locking effect even for highly distorted meshes.

In this example it is necessary to treat another locking effect, the Poisson thickness locking, with at least linear distribution of the thickness strains. Both solid shell elements use an enhanced assumed strain distribution in thickness direction to relieve this looking effect. However, the diagram Fig. 5 shows that the present solid shell leads to slightly larger deflections than the Q1A3E7 element.

5.3 Cook's membrane problem

This geometrically and physically non–linear example was proposed in [33]. A trapezoidal membrane is clamped on one side while the other side is loaded, see Fig. 6. The Neo–Hookean material model, see Appendix A.1, is applied for the constitutive law; the shear modulus μ and the Lamé constant Λ are given in Fig. 6. For a large value of Λ the Lamé constant can be interpreted as a penalty factor and the incompressibility is approximately fulfilled.

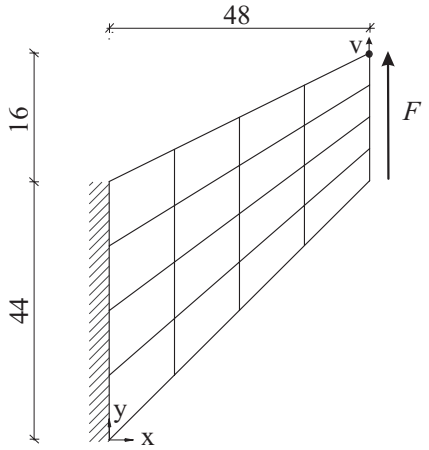

Material data:

$\Lambda = 40.0889 \cdot 10^4$

$\mu = 80.1938$

Thickness:

$t = 1$

Fig. 6. Cook's membrane: geometrical and material properties

The computation is performed using load control with load steps of $\Delta F = 1.0$ from $F = 0$ up to $F = 100$. Fig. 7 shows the vertical displacement of the top edge node plotted versus the number of elements per side of the different meshes. For the presented HSEE solid shell element only one element through the thickness is considered, which holds also for the Q1A3E7 element. The deflections are compared to those of the enhanced four node plane strain element Q1E4 proposed in [33]. All three formulations converge to the same result. The present formulation exhibits much better accuracy for coarse meshes, whereas

load increment	iteration	Simo, Armero [33]	HSEE solid shell
$\Delta F = 1$	1	$3.5078038 \cdot 10^{-1}$	$1.7399264 \cdot 10^{-1}$
$F = 0 \rightarrow F = 1$	2	$9.8340487 \cdot 10^{+1}$	$2.3341304 \cdot 10^{+1}$
	3	$2.9872313 \cdot 10^{-3}$	$6.7990261 \cdot 10^{-5}$
	4	$7.3419459 \cdot 10^{-5}$	$4.0356002 \cdot 10^{-8}$
	5	$2.5837469 \cdot 10^{-9}$	
load increment	iteration	Q1A3E7	HSEE solid shell
$\Delta F = 10$	1	$1.7399264 \cdot 10^{+0}$	$1.7399264 \cdot 10^{+0}$
$F = 90 \rightarrow F = 100$	2	$2.0283293 \cdot 10^{+3}$	$1.6486545 \cdot 10^{+3}$
	3	$1.8706805 \cdot 10^{+1}$	$4.1416162 \cdot 10^{-1}$
	4	$1.8146389 \cdot 10^{+1}$	$4.9356821 \cdot 10^{-3}$
	5	$5.2998562 \cdot 10^{-2}$	$4.0496369 \cdot 10^{-8}$
	6	$1.7113390 \cdot 10^{-4}$	
	7	$3.9370601 \cdot 10^{-8}$	
$\Delta F = 100$	1	no convergence	$1.7399264 \cdot 10^{+1}$
$F = 0 \rightarrow F = 100$	2		$2.4535562 \cdot 10^{+5}$
	3		$5.6068275 \cdot 10^{+3}$
	4		$2.0163798 \cdot 10^{+3}$
	5		$1.8824028 \cdot 10^{+1}$
	6		$1.4375709 \cdot 10^{+0}$
	7		$1.5296451 \cdot 10^{-3}$
	8		$5.9077728 \cdot 10^{-8}$

Table 2
Convergence of the Euclidian norm of the residual vector during equilibrium iteration

the results of the Q1A3E7 and the Q1E4 are nearly identical. The deformed configuration consisting of $32 \times 32 \times 1$ elements is shown in Fig. 7.

In Tab. 2 the norm of the residual vector for different load increments is summarized. It demonstrates the superior convergence behavior of the present formulation especially for large load increments in comparison to the Q1A3E7 element.

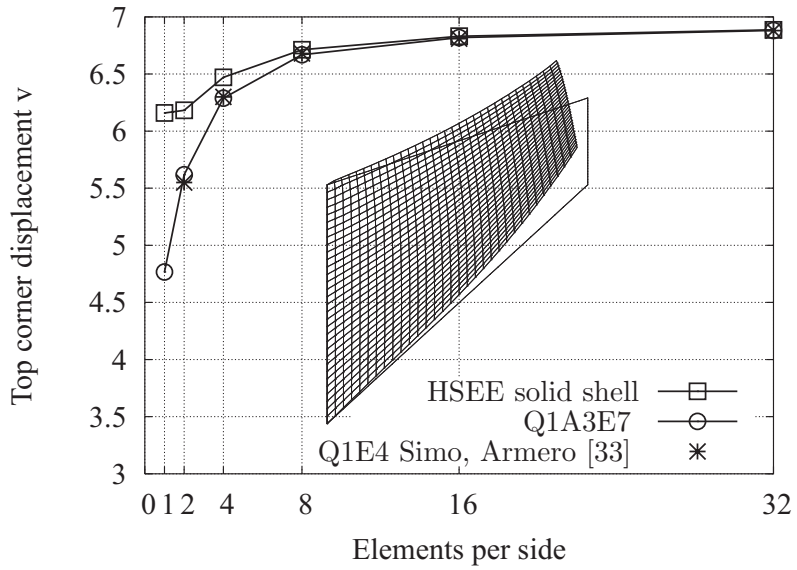

Fig. 7. Cook's membrane: convergence of the finite element solutions with comparison of different element formulations

5.4 Hemisphere with 18^o *hole*

This geometrically non-linear example is often cited as a benchmark for shell elements, see e.g. [36], and is a test for the ability to model rigid body modes and inextensible bending. The shell is subjected to four single loads, see Fig. 8. Here R is the radius of the shell middle surface and t denotes the thickness. The St.-Venant-Kirchhoff material is characterized by Young's modulus E and Poisson's ratio ν. With respect to symmetry only a quarter of the system is modelled with 16×16 finite elements in plane and with one element through the thickness.

The pinching forces are increased up to a load $F = 2.5$ in 20 equal-sized load increments. In Fig. 9 the inward and outward displacements at the points A and B are plotted versus the pinching load F. The solid shell element provides no node in the middle surface of the shell, therefore the associated displacements are calculated by averaging the displacements of the inner and outer surface, see the detail in Fig. 8.

To assess the convergence behavior the results are compared to shell elements proposed in [3, 14, 23, 43]. In [3, 43] the quarter of the system is modelled by 16×16 four node shell elements. Parisch [23] introduced 8×8 shell elements with quadratic shape functions. For the solid shell element Q1A3E5 proposed in [14] the same finite element discretization is employed as for the present one. Our solution agrees very well with the one in [43], which is based on a zero normal stress condition and therefore is free of curvature thickness locking and Poisson locking effects.

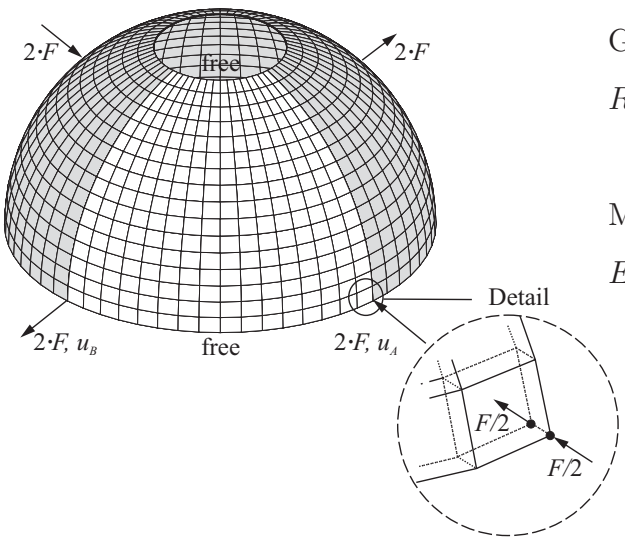

Geometry data:

$R = 10 \qquad t = 0.01$

Material data:

$E = 6.825 \cdot 10^7 \;\; \nu = 0.3$

Fig. 8. Finite element model of the hemisphere with hole; loading points at the quarter of the system

To investigate the differences in the load deflection curves depicted in Fig. 9 a convergence study has been accomplished. The present element as well as the elements from [14, 43] lead to the same results for a $64 \times 64 \times 1$ finite element mesh. A further mesh refinement does not change the displacement response significantly. Furthermore, the load deflection diagram in Fig. 9 shows that the present element converges faster against the correct solution than the elements [3, 14, 23].

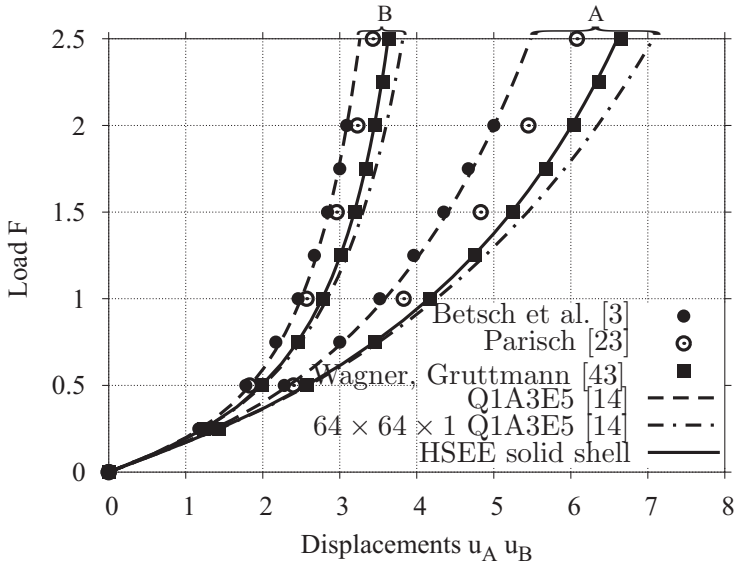

Fig. 9. Load deflection diagram for the displacements u_A and u_B

To demonstrate another advantage of the present formulation the convergence rate of the equilibrium iteration is examined. In Tab. 3 the equilibrium iterations for different load steps are listed. If a load $F = 0.125$ is applied to

load increment	iteration	Q1A3E5	HSEE solid shell
$\Delta F = 0.125$	1	$1.2500000 \cdot 10^{-1}$	$1.2500000 \cdot 10^{-1}$
$F = 0 \rightarrow F = 0.125$	2	$6.9991349 \cdot 10^{+6}$	$7.0184158 \cdot 10^{+6}$
	3	$8.0648375 \cdot 10^{+4}$	$9.1423844 \cdot 10^{+4}$
	4	$1.9094676 \cdot 10^{+4}$	$1.8102654 \cdot 10^{+1}$
	5	$1.0493687 \cdot 10^{+3}$	$5.6128239 \cdot 10^{-5}$
	6	$7.4607803 \cdot 10^{+2}$	
	7	$4.7130570 \cdot 10^{+2}$	
	8	$3.6091711 \cdot 10^{+2}$	
	9	$2.2958236 \cdot 10^{+2}$	
	10	$2.1759446 \cdot 10^{+2}$	
	11	$9.2434598 \cdot 10^{+1}$	
	12	$1.0077155 \cdot 10^{+2}$	
	13	$1.8389587 \cdot 10^{+1}$	
	14	$1.1024285 \cdot 10^{+1}$	
	15	$2.4866909 \cdot 10^{-1}$	
	16	$2.4364768 \cdot 10^{-3}$	
	17	$5.1168022 \cdot 10^{-5}$	
$\Delta F = 2.5$	1	no convergence	$2.5000000 \cdot 10^{+0}$
$F = 0 \rightarrow F = 2.5$	2		$6.6981264 \cdot 10^{+9}$
	3		$9.6238530 \cdot 10^{+8}$
	4		$1.8512449 \cdot 10^{+8}$
	5		$2.4455530 \cdot 10^{+7}$
	6		$1.4298378 \cdot 10^{+6}$
	7		$1.3248578 \cdot 10^{+5}$
	8		$1.3781622 \cdot 10^{+2}$
	9		$4.1150342 \cdot 10^{-4}$
	10		$3.8434455 \cdot 10^{-5}$

Table 3
Convergence of the residuum during equilibrium iteration

the initial system, the solid shell element Q1A3E5 needs 17 iterations to obtain equilibrium, whereas the present HSEE solid shell element converges in 5 steps. If the total load $F = 2.5$ is applied in one single step, the HSEE solid

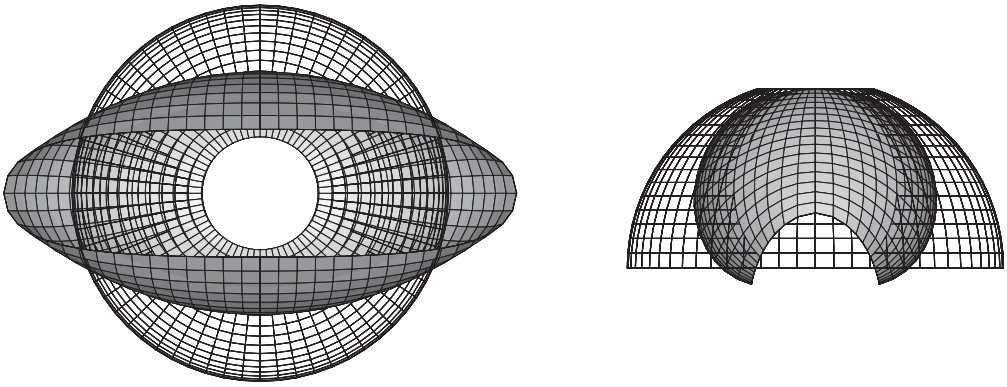

Fig. 10. Deformed structure at $\lambda = 1$

shell formulation needs 10 iterations to find equilibrium and the Q1A3E5 does not converge. The deformed finite element mesh using the present element formulation is shown in Fig. 10.

5.5 Full hemispherical shell

The structure examined here is shown in Fig. 11 and was introduced in [34]. The elastic–plastic material behavior is modelled by a finite strain elastic-plastic material description, which is summarized in Appendix A.2. The example illustrates the excellent convergence behavior of the presented element formulation in a geometrical and physical non-linear range for large load steps. Furthermore it shows the good agreement of the displacement response with other shell elements.

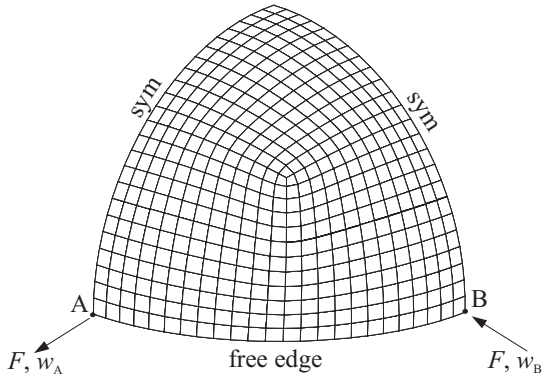

Geometry:

$R = 10$

$t = 0.5$

Material:

$E = 10$

$\nu = 0.2$

$y_0 = 0.2$

$h = 0$

Fig. 11. The cantilever rod with boundary conditions and material properties

The elastic and plastic material parameters and the geometrical data are listed in Fig. 11. Here, E, ν, y_0, h are Young's modulus, Poisson's ratio, initial yield stress and linear hardening parameter. The radius R is defined with respect to the middle surface of the shell and the thickness is denoted by t. Considering symmetry only a quarter of the system is modelled with 24 elements per side in the shell plane and one element through the thickness. The structure is

loaded at the points A and B with an inward and outward concentrated load F. The load is applied according to the detail in Fig. 8.

The computed load deflection diagram for the displacements w_A and w_B is depicted in Fig. 12. For the points A and B it is distinguished between the displacements at the inner node and at the outer node. The diagram demonstrates a good agreement of the presented element formulation HSEE solid shell with the Q1A3E7 element and the shell element introduced in [4].

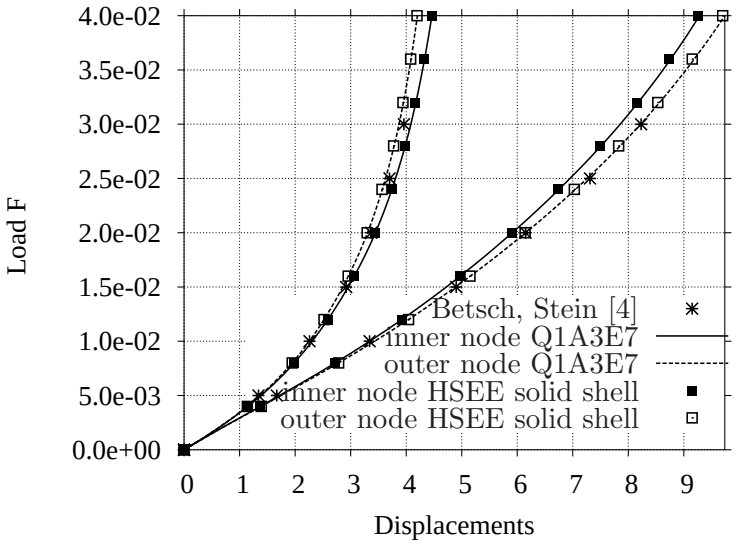

Fig. 12. Load deflection diagram for inward and outward displacements

The robustness of the proposed element formulation is examined applying different load increments ΔF to the initial system. The norm of the residual vector within the equilibrium iteration is shown in Tab. 4. For a large load step $\Delta F = 4.5 \cdot 10^{-3}$ the proposed element formulation needs only 6 iteration steps to obtain equilibrium. In contrast to that the enhanced assumed strain formulation Q1A3E7 needs 13 iteration steps. It is noted that for a very large load increment $\Delta F = 40 \cdot 10^{-3}$ the presented element formulation converges within 9 steps, whereas no equilibrium state is found with the Q1A3E7 formulation.

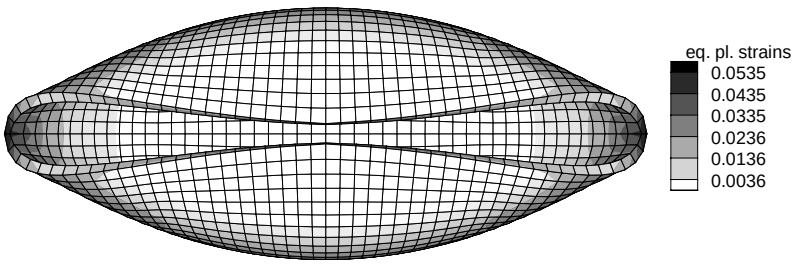

Fig. 13. Deformed structure at $F = 40 \cdot 10^{-3}$ with a plot of equivalent plastic strains

For the total load $F = 40 \cdot 10^{-3}$ the deformed structure with a plot of the equivalent strains is depicted in Fig. 13, where the load is increased by a load step $\Delta F = 1 \cdot 10^{-3}$. It is found that the maximum of the equivalent plastic

load increment	iteration	Q1A3E7	HSEE solid shell
$\Delta F = 1 \cdot 10^{-3}$	1	$1.0000000 \cdot 10^{-03}$	$1.0000000 \cdot 10^{-03}$
$F = 0 \rightarrow F = 1 \cdot 10^{-3}$	2	$1.0255057 \cdot 10^{-01}$	$1.0304972 \cdot 10^{-01}$
	3	$1.4620802 \cdot 10^{-04}$	$1.6758631 \cdot 10^{-04}$
	4	$1.6814215 \cdot 10^{-06}$	$3.1458114 \cdot 10^{-10}$
	5	$1.1589160 \cdot 10^{-12}$	$1.2193957 \cdot 10^{-13}$
$\Delta F = 4.5 \cdot 10^{-3}$	1	$4.5000000 \cdot 10^{-03}$	$4.5000000 \cdot 10^{-03}$
$F = 0 \rightarrow F = 4.5 \cdot 10^{-3}$	2	$1.9717494 \cdot 10^{+00}$	$2.1299179 \cdot 10^{+00}$
	3	$2.6660921 \cdot 10^{-01}$	$6.1554178 \cdot 10^{-02}$
	4	$5.8287892 \cdot 10^{-01}$	$5.2909746 \cdot 10^{-05}$
	5	$1.1760770 \cdot 10^{-01}$	$3.5602566 \cdot 10^{-11}$
	6	$3.0378222 \cdot 10^{-01}$	$1.1944998 \cdot 10^{-13}$
	7	$8.9652086 \cdot 10^{-02}$	
	8	$7.1431481 \cdot 10^{-02}$	
	9	$5.1928597 \cdot 10^{-02}$	
	10	$7.1564570 \cdot 10^{-03}$	
	11	$1.7397217 \cdot 10^{-05}$	
	12	$2.8206958 \cdot 10^{-10}$	
	13	$1.2215279 \cdot 10^{-13}$	
$\Delta F = 40 \cdot 10^{-3}$	1	no convergence	$4.0000000 \cdot 10^{-02}$
$F = 0 \rightarrow F = 40 \cdot 10^{-3}$	2		$3.2168768 \cdot 10^{+02}$
	3		$4.7483025 \cdot 10^{+01}$
	4		$1.1718805 \cdot 10^{+01}$
	5		$2.4045442 \cdot 10^{+00}$
	6		$5.4100507 \cdot 10^{-02}$
	7		$4.7898365 \cdot 10^{-05}$
	8		$7.7575103 \cdot 10^{-11}$
	9		$1.0356731 \cdot 10^{-13}$

Table 4
Convergence of the norm of the residual vector during an equilibrium iteration

strain $\approx 5.35\%$ appears at point A. The implicit integration algorithm to solve the set of elastic–plastic material equations is an approximative procedure and leads for larger load steps in general to a loss of accuracy. In the present case

if one applies the total load in one step $\Delta F = 40 \cdot 10^{-3}$ however no significant differences neither in the displacements nor in the equivalent plastic strains are noted.

5.6 Conical shell

This example is selected to demonstrate the ability of the developed finite element to deal with strongly non-linear situations. The geometrical data are taken from Başar and Itskov [1], who investigated this problem using an Ogden material. Here, elastic–plastic material behavior is assumed. The material model for finite plastic strains is summarized in Appendix A.2. All necessary material and geometrical data are depicted in Fig. 14. Regarding to [1] the problem is slightly modified due to eccentric loading and boundary conditions.

Considering symmetry, only a quarter of the shell is discretized with $16 \times 16 \times 1$ elements. Thus only symmetric buckling behavior may occur. The nonlinear behavior is computed using an arclength algorithm with displacement control. The results are depicted in Fig. 15, where w denotes the vertical displacement of the upper edge. The load deflection diagram demonstrates that the displacement response of the present formulation and the enhanced assumed strain formulation Q1A3E7 agree very well.

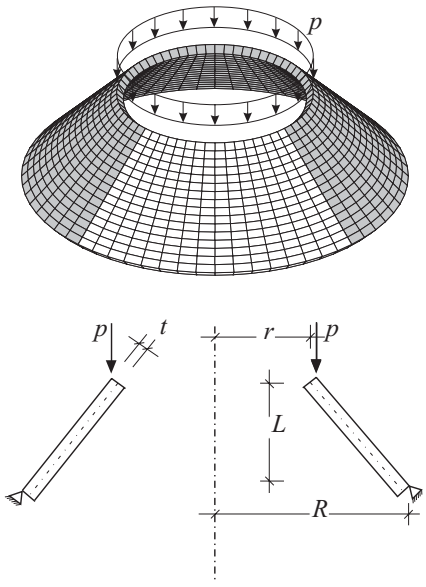

Geometry:	Material:
$r = 1$	$E = 206.9$
$R = 2$	$\nu = 0.29$
$L = 1$	$\sigma_y = 0.45$
$t = 0.1$	$\sigma_\infty = 0.715$
Load: p	$h = 0.12924$
	$\eta = 16.93$

Fig. 14. Finite element mesh with geometrical and material data

The load is increased until $w = 0.02$, where the elastic limit load is reached. Hence a rolling process starts at the top of the conical shell. A further stability point is traced at $w = 1.08$. Here, a global snap through behavior is observed. A local minimum of the load defection curve is attained at $w = 1.67$. Then a

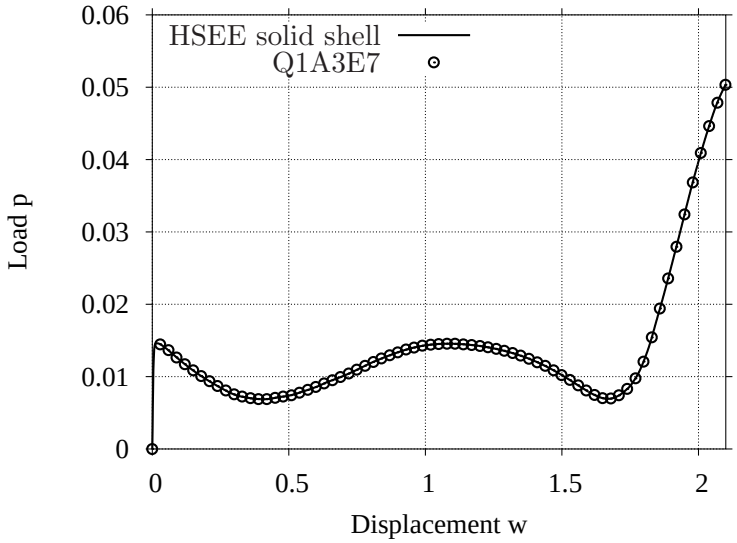

Fig. 15. Load deflection diagram: the load p versus the vertical displacement w of the upper outer edge

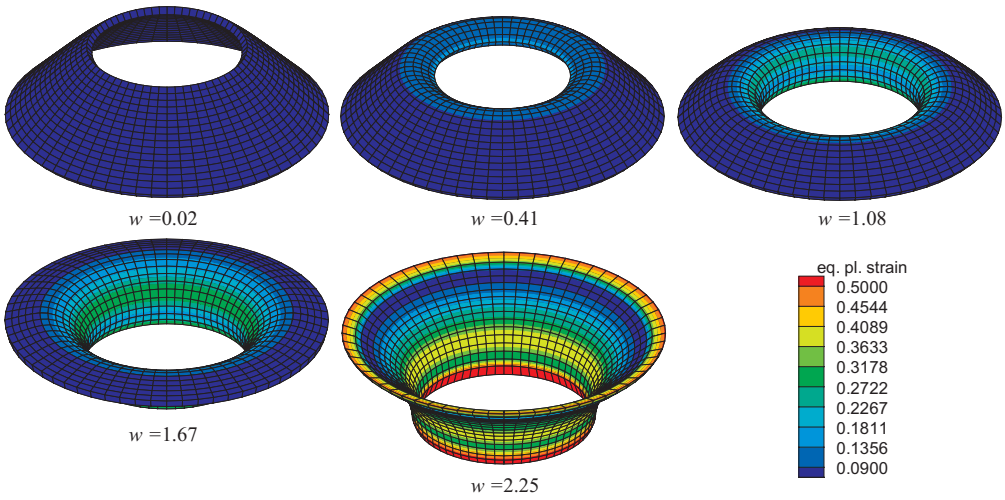

Fig. 16. Deformed meshes with a plot of the equivalent plastic strains

stable path with increasing loads due to stiffening effects arises. The deformed meshes at characteristic points are shown in Fig. 16.

A Appendix

In the following we briefly summarize the basic equations of the material models used in the examples.

A.1 Hyper-elastic material

Following [22, 41] the strain energy function is given by

$$W_{0S} = [\frac{\mu}{2}(\lambda_1^2 + \lambda_2^2 + \lambda_3^2 - 3) - \mu \ln(J)] + \frac{\Lambda}{4}(J^2 - 1 - 2 \ln(J)) \tag{A.1}$$

with

$$J = \lambda_1 \lambda_2 \lambda_3 \quad . \tag{A.2}$$

Here λ_i are the principal stretches of the elastic material, which are evaluated by solving the eigenvalue problem

$$(\boldsymbol{C} - \lambda_A^2 \mathbf{1}) \boldsymbol{N}^A = \mathbf{0} \quad \text{with} \quad A = 1, 2, 3 \quad . \tag{A.3}$$

Furthermore $\boldsymbol{N}^A$ denotes the eigenvector and with Eq. (3) the right Cauchy-Green tensor $\boldsymbol{C}$ is obtained from

$$\boldsymbol{C} = 2\bar{\boldsymbol{E}} - \mathbf{1} \quad . \tag{A.4}$$

The material parameter Λ is a Lamé constant, which may be computed from the shear modulus μ and the bulk modulus κ as $\Lambda = \kappa - 2/3\mu$. For a large value of Λ the Lamé constant can be interpreted as a penalty factor and the incompressibility condition is approximately fulfilled, $\det \boldsymbol{F} = \lambda_1 \lambda_2 \lambda_3 \approx 1$.

A.2 Finite strain J_2-plasticity model

The applied plasticity model for finite strains is restricted to isotropic material behavior. The numerical realization of the finite strain J_2-plasticity model is proposed in several papers; see e.g. [31], [20] and the references therein. The finite deformation plasticity model is based on a multiplicative decomposition of the deformation gradient $\boldsymbol{F} = \boldsymbol{F}^e \, \boldsymbol{F}^p$ in an elastic and plastic part. Due to the Lagrangean formulation of the variational equations the plasticity model is formulated using the right Cauchy-Green tensor according to Eq. (A.4). With $\boldsymbol{C}^p = \boldsymbol{F}^{p\,T} \boldsymbol{F}^p$ the eigenvalue problem

$$(\boldsymbol{C} - \lambda_A^{e\,2} \boldsymbol{C}^p) \, \hat{\boldsymbol{N}}^A = \mathbf{0} \quad \text{with} \quad \hat{\boldsymbol{N}}^A \cdot \boldsymbol{C}^p \, \hat{\boldsymbol{N}}^B = \delta^{AB} \tag{A.5}$$

yields the elastic stretches λ_A^e. The elastic strain energy function is defined as

$$W_{el} = \frac{\Lambda}{2}[\varepsilon_1^e + \varepsilon_2^e + \varepsilon_3^e]^2 + \mu[(\varepsilon_1^e)^2 + (\varepsilon_2^e)^2 + (\varepsilon_3^e)^2] \quad \text{with} \quad \varepsilon_A = ln[\lambda_A^e] \quad . \tag{A.6}$$

Here Λ and μ are material parameters. The evolution law of the plastic strains and the internal variable are derived from the principle of maximum plastic

dissipation; see [32]. A Lagrangean formulation of the plastic flow rule is given as

$$\dot{\boldsymbol{C}}^p = 2\,\lambda\,\boldsymbol{C}^p\,(\boldsymbol{F}^{-1}\,\frac{\partial\phi}{\partial\boldsymbol{\tau}}\boldsymbol{F}) \qquad , \qquad \dot{\alpha} = \lambda\,\frac{\partial\phi}{\partial q} \tag{A.7}$$

where λ denotes the Lagrange multiplier, $\boldsymbol{\tau}$ is the Kirchhoff stress and α, q are conjugate internal hardening variables. The yield criterion ϕ is of a von Mises type with exponential isotropic hardening, [21]

$$\phi = \sqrt{\frac{3}{2}\,\boldsymbol{\tau}^D\cdot\boldsymbol{\tau}^D} - (y_0 + h\,\alpha + (y_\infty - y_0)(1-\exp[-\eta\,\alpha])) \quad . \tag{A.8}$$

In this equation h, y_0, y_∞, η are material parameters and $\boldsymbol{\tau}^D$ is the deviatoric Kirchhoff stress tensor. An implicit exponential integration algorithm of the evolution equations (A.7) along with the strain energy (A.6), introduced in [31], leads to an additive model as in the linear theory.

References

[1] Y. Başar, M. Itskov, Finite element formulation of the Ogden material model with application to rubber-like shells, Int. J. Num. Meth. Eng. 42 (1998) 1279–1305.

[2] P. Betsch, F. Gruttmann, E. Stein, A 4–node finite shell element for the implementation of general hyperelastic 3d–elasticity at finite strains, Comp. Meth. Appl. Mech. Eng. 130 (1996) 57–79.

[3] P. Betsch, E. Stein, An assumed strain approach avoiding artificial thickness straining for a nonlinear 4–node shell element, Commun. Num. Meth. Eng. 11 (1995) 899–909.

[4] P. Betsch, E. Stein, Numerical implementation of multiplicative elasto-plasticity into assumed strain elements with application to shells at large strains, Comp. Meth. Appl. Mech. Eng. 179 (3–4) (2000) 215–246.

[5] M. Bischoff, E. Ramm, Shear deformable shell elements for large strains and rotations, Int. J. Num. Meth. Eng. 40 (1997) 4427–4449.

[6] M. Bischoff, E. Ramm, D. Braess, A class of equivalent enhanced assumed strain and hybrid stress finite elements, Comp. Mech. 22 (1999) 443–449.

[7] N. Büchter, E. Ramm, D. Roehl, Three–dimensional extension of nonlinear shell formulation based on the enhanced assumed strain concept, Int. J. Num. Meth. Eng. 37 (1994) 2551–2568.

[8] E. Dvorkin, K. Bathe, A continuum based four–node shell element for general nonlinear analysis, Eng. Comp. 1 (1984) 77–88.

[9] R. Eberlein, P. Wriggers, Finite element formulations of 5– and 6–parameter shell theories accounting for finite plastic strains, in: D. Owen, E. Onate, E. Hinton (Eds.), Computational Plasticity, Fundamentals and Applications, CIMNE, Barcelona, 1997, pp. 1898–1903.

[10] R. Hauptmann, K. Schweizerhof, A systematic development of 'solid-shell' element formulations for linear and non-linear analyses employing only displacement degrees of freedom, Int. J. Num. Meth. Eng. 42 (1) (1998) 49–69.

[11] T. Hughes, T. Tezduyar, Finite elements based upon mindlin plate theory with reference to the four-node isoparametric element, J. Appl. Mech. 48 (1981) 587–596.

[12] E. Kasper, R. Taylor, A mixed-enhanced strain method part i: Geometrically linear problems, Comput. & Struct. 75 (2000) 237–250.

[13] E. Kasper, R. Taylor, A mixed-enhanced strain method part ii: Geometrically nonlinear problems, Comput. & Struct. 75 (2000) 251–260.

[14] S. Klinkel, F. Gruttmann, W. Wagner, A continuum based three-dimensional shell element for laminated structures, Comput. & Struct. 71 (1999) 43–62.

[15] S. Klinkel, W. Wagner, A geometrical non-linear brick element based on the EAS–method, Int. J. Num. Meth. Eng. 40 (1997) 4529–4545.

[16] M. Loikkannen, B. Irons, An 8-node brick finite element, Int. J. Num. Meth. Eng. 20 (1983) 523–528.

[17] R. MacNeal, A simple quadrilateral shell element, Comput. & Struct. 8 (1978) 175–183.

[18] R. MacNeal, R. Harder, A proposed standard set of problems to test finite element accuracy, Finite Elemets in Analysis and Design 1 (1985) 3–20.

[19] C. Miehe, A theoretical and computational model for isotropic elastoplastic stress analysis in shells at large strains, Comp. Meth. Appl. Mech. Eng. 155 (1998) 193–223.

[20] C. Miehe, E. Stein, A canonical model of multiplicative elasto-plasticity formulation and aspects of the numerical implementation, European J. of Mech. A 11 (1992) 25–43.

[21] R. Mises, Mechanik der plastischen Formänderung von Metallen, Zeitschrift für angewandte Mathematik und Mechanik 8 (3) (1928) 161–185.

[22] R. Ogden, Large deformation isotropic elasticity – on the correlation of theory and experiment for compressible rubberlike solids, Proc. Royal Soc. London A328 (1972) 567–583.

[23] H. Parisch, A continuum-based shell theory for non-linear applications, Int. J. Num. Meth. Eng. 38 (1995) 1855–1883.

[24] T. Pian, K. Sumihara, Rotational approch for assumed stress finite elements, Int. J. Num. Meth. Eng. 20 (1984) 1685–1695.

[25] T. Pian, P. Tong, Relationship between incompatible displacement model and hybrid stress model, Int. J. Num. Meth. Eng. 22 (1986) 173–181.

[26] R. Piltner, Low order plate bending elements with enhanced strains, Comput. & Struct. 80 (2002) 849–856.

[27] R. Piltner, R. Taylor, A systematic construction of b-bar functions for linear and non-linear mixed-enhanced finite elements for plane elasticity problems, Int. J. Num. Meth. Eng. 44 (1999) 615–639.

[28] E. Ramm, M. Bischoff, M. Braun, Higher order nonlinear shell formulations – a step back into three dimensions, in: T. K. Bell, Dept. of Structural Engineering Institute of Technology (Ed.), From Finite Elements to the Troll Platform, Norway, 1994, pp. 65–88.

[29] H. Schoop, Oberflächenorientierte Schalentheorien endlicher Verschiebungen, Ingenieur Archiv 56 (1986) 427–437.

[30] D. Shenglin, E. Ramm, On alternative hybrid stress 2d and 3d elements, Eng. Comp. 11 (1) (1994) 49–68.

[31] J. Simo, Algorithms for static and dynamic multiplicative plasticity that preserve the classical return mapping schemes of the infinitesimal theory, Comp. Meth. Appl. Mech. Eng. 99 (1992) 61–112.

[32] J. Simo, Numerical analysis of classical plasticity, in: P. Ciarlet, J. Lions (Eds.), Handbook of Numerical Analysis, North-Holland, 1998.

[33] J. Simo, F. Armero, Geometrically non-linear enhanced strain mixed methods and the method of incompatible modes, Int. J. Num. Meth. Eng. 33 (1992) 1413–1449.

[34] J. Simo, J. Kennedy, On a stress resultant geometrically exact shell model. part v. nonlinear plasticity: Formulation and integration algorithms, Comp. Meth. Appl. Mech. Eng. 96 (1992) 133–171.

[35] J. Simo, M. Rifai, A class of mixed assumed strain methods and the method of incompatible modes, Int. J. Num. Meth. Eng. 29 (1990) 1595–1638.

[36] J. Simo, M. Rifai, D. Fox, On a stress resultant geometrically exact shell model. part iv: Variable thickness shells with through–the–thickness stretching, Comp. Meth. Appl. Mech. Eng. 81 (1990) 91–126.

[37] W. Sprenger, F. Gruttmann, W. Wagner, Delamination growth analysis in laminated structures with continuum based 3d-shell elements and a viscoplastic softening model, Comp. Meth. Appl. Mech. Eng. 185 (2000) 123–139.

[38] K. Sze, L. Yao, A hybrid stress ANS solid-shell element and its generalization for smart structure modelling. part i – solid-shell element formulation, Int. J. Num. Meth. Eng. 48 (2000) 545–564.

[39] R. Taylor, Feap - manual, http:\\www.ce.berkeley \ ∼ rlt \ feap \ manual.pdf.

[40] S. Timoshenko, S. Woinowsky-Krieger, Theory of Plates and Shells, 2nd Edition, McGraw-Hill, New York, 1970.

[41] L. Treloar, Stress-strain data for vulcanised rubber under various types of deformation, Trans. Farady Soc. 40 (1944) 59–70.

[42] L. Vu-Quoc, X. Tan, Optimal solid shell for non-linear analyses of multilayer composites. I. statics, Comp. Meth. Appl. Mech. Eng. 192 (2003) 975–1016.

[43] W. Wagner, F. Gruttmann, On efficient FE-formulations in the stability analysis of thin-walled structures, in: Sixth World Congress on Computational Mechanics, WCCM VI, Beijing, China, 2004.

[44] W. Wagner, S. Klinkel, F. Gruttmann, Elastic and plastic analysis of thin-walled structures using improved hexahedral elements, Comput. & Struct. 80 (2002) 857–869.